https://arabjchem.org

ScientificScholar®
Knowledge is power
Publisher of Scientific Journals

Arabian Journal of Chemistry

Article in Press

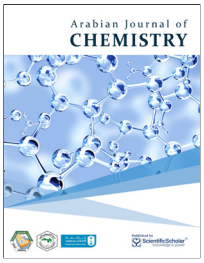

Original Article

Ferromagnetic nature and solar-induced fast catalytic properties for green environment: New Fe/Cu/V-Mn_3O_4 p-type compounds

Ghayah Mohammed Alsulaim*

Department of Chemistry, Faculty of Science, King Faisal University, Al-Ahsa, 31982, Saudi Arabia

ARTICLE INFO

Keywords:
Magnetic properties
Optical features
Removal of organic contaminants
Spin-devices
Visible-light band gap

ABSTRACT

Nanocrystalline pure, Fe-Cu and Fe-V substituted Mn_3O_4 semiconductors were produced via a coprecipitation process as advanced magnetic compositions and efficient photocatalysts for the elimination of industrial Congo red (CR) waste. The X-ray diffraction (XRD) results confirmed that all samples have a tetragonal structure of Mn_3O_4 (hausmannite, I41/amd). The band gap energy of pure, Fe-Cu, and Fe-V co-doped Mn_3O_4 nanostructures were measured to be 2.1, 1.78, and 1.65 eV, respectively. The valence states of Cu, Fe, and V cations were confirmed by the X-ray photoelectron spectroscopy (XPS) as +2, +3, and +4, respectively. The magnetic analysis of Fe-Cu and Fe-V co-doped Mn_3O_4 powders gives room temperature hysteresis ferromagnetic curves. The obtained magnetic data demonstrated a spin-ferromagnetic order as Fe^{3+}-Cu^{2+} and Fe^{3+}-V^{4+} cations replaced Mn-sites inside Mn_3O_4 structure with measured saturation magnetization of 1.49 and 1.67 emu/g as well as coercivity of 1668 and 378 Oe, respectively. Both Fe^{3+}-Cu^{2+} and Fe^{3+}-V^{4+} mixtures, as well as the oxygen vacancies, are accountable for the ferromagnetic nature according to the bound magnetic polarons (BMPs) visualization. The Fe^{3+}-Cu^{2+} substituted Mn_3O_4 semiconductor as a photocatalyst revealed a rapid solar photo-removal activity of 98% after 25 mins when applied to remove CR as industrial waste.

1. Introduction

In the last few decades, p-type semiconducting manganese oxide (Mn_3O_4) was candidate as a practical material for many applications, such as supercapacitors [1,2], lithium-ion batteries [3,4], removal of pollutants by photocatalysis [5,6], hydrogen production [7], gas sensors [8,9], and future spin-information devices [10-12], owing to its interesting structural flexibility and important chemical and physical properties. Mn_3O_4 is a well-known p-type semiconductor with a band gap energy of 2.2-2.8 eV. Besides, it has good chemical stability, relatively high conductivity and high thermodynamic stability while being cheap, ecofriendly, and readily available [13,14]. Lately, the preparation and the magnetic characteristics of the pure nanostructured Mn_3O_4 semiconductor have attracted great interest, particularly in the forms of quantum dots, nanoparticles, and nanowires/rods [12,15-17]. The development of magnetic properties of the Mn_3O_4 semiconductor is useful for magnetic resonance imaging (MRI) and spin-memory devices [18,19]. As is recognized to all, doping and co-doping techniques into oxide materials, with a good selection of transition or rare earth elements as cation-dopants, offers operative routes to regulate their magnetic characteristics, which is critical for numerous practical applications [12,20-22]. Up to the present time, reports on the synthesis and magnetic characteristics of doped and co-doped Mn_3O_4 nanostructures are limited. For example, Raja *et al.* reported that a 3% Ni doped Mn_3O_4 composition has a ferromagnetic order at room temperature with measured saturation magnetization of 0.008364 emu/g [20]. The prepared Mn_3O_4 quantum dots exhibit room temperature ferromagnetism with saturation magnetization and remanence values of 0.366 emu/g and remanence 0.073 emu/g [15].

In our time, one of the vital problems of industries, such as the textile and paper industries, is the hazardous waste and contamination of water systems [23,24]. It was reported that billions of people don't have access to pure and clean water, increasing the risk of using contaminated water [25,26]. The uncontrolled discharge of colored organic waste, such as synthetic dyes or pesticides has caused dangerous environmental contamination [27,28]. Therefore, the degradation and removal of organic pollutants with advanced and effective wastewater treatment techniques is a vital issue from the point of view of security and public health [29,30]. Manganese oxides are strong candidates as functional catalysts for the treatment of dissolved pollutants owing to their low cost, non-toxicity, optical properties, innovative chemical-physical characteristics, and numerous structures (MnO, MnO_2, Mn_2O_3, and Mn_3O_4) [31-33]. The semiconducting Mn_3O_4 structure is an important and best-known catalyst owing to Mn vacancies and its attractive optical characteristics [34-36].

Rani *et al.* [37] stated that Mn_3O_4 nanoparticles synthesized from the Curry leaf (Murraya Koenigii) extract exhibit a photodegradation efficiency of 94% towards the Rhodamine B (RhB) dye after 110 mins under UV-visible light irradiation. The prepared Mn_3O_4 nanotube has shown a visible light photo-removal activity of 80% for amido black 10B dye after 60 mins [38]. Sheikhshoaie *et al.* [39] revealed that thallium (Tl)-doped Mn_3O_4 catalyst has a photocatalytic activity of 84% for the methylene blue dye after a reaction time of 30 mins, powered by sunlight activation. Al_2O_3-doped Mn_3O_4 nanomaterial was used

*Corresponding author:
E-mail address: galsaleem@kfu.edu.sa (G. Alsulaim)

Received: 12 February, 2025 **Accepted:** 05 April, 2025 **Epub Ahead of Print:** 30 May 2025 **Published:** ***
DOI: 10.25259/AJC_134_2025

for the removal of brilliant cresyl blue, with a recorded degradation efficiency of ~ 65% under visible light irradiation for 5 hrs [40]. A visible light removal efficiency of 75% was reported for 12% zinc-doped Mn_3O_4 nanoparticles towards methylene blue pollutant over 75 mins [41]. Nickel (Ni)-doped Mn_3O_4 nanoparticle as a photocatalyst material exhibited a photo-activity of 98% against methylene blue after 150 mins [42].

The published reports on the modified Mn_3O_4 semiconductor illustrated that the using of Fe-Cu and Fe-V cations have rarely been studied. The suitability of Fe, Cu, and V ions as dopants for Mn_3O_4 structure related to the matching in ionic size as well as these elements have numerous oxidation states with interesting electronic configurations. The original goal of this research was to synthesize pure, Fe-Cu, and Fe-V co-doped Mn_3O_4 nanoparticles using a simplistic chemical coprecipitation method to advance their magnetic and photocatalytic applications. This synthesis process is cheap, straight, and can be simply fixed for the manufacture of a large mass of nanomaterials. The incorporation of Fe-Cu and Fe-V cations was functionalized to develop the room temperature ferromagnetic properties of the Mn_3O_4 semiconductor for technological uses. Furthermore, the synthesized compositions were used as solar-sensitive catalysts for organic waste elimination produced from industrial effluents. The structural characterization, optical properties, and particles morphology of the produced nanopowders were studied through X-ray diffraction (XRD), X-ray photoelectron spectroscopy (XPS), high resolution-transmission electron microscopy (HR-TEM), and diffuse reflectance (DR) apparatuses, respectively.

2. Materials and Methods

2.1. Synthesis procedure

To synthesise pure Fe-Cu, and Fe-V substituted Mn_3O_4 nanoparticles (Hausmannite), highly analytical grade chemical reagents were utilized without further purification. $MnCl_2{\cdot}4H_2O$, $Cu(NO_3)_2{\cdot}3H_2O$, $Fe(NO_3)_2{\cdot}9H_2O$, and NH_4VO_3 were used as sources for Mn, Fe, Cu, and V, with NaOH as the precipitating agent. Milli-Q Water was used as a solvent during the chemical reaction to synthesise pure, Fe-Cu, and Fe-V co-doped Mn_3O_4 compositions [43,44]. For the synthesis process, required amounts of chemical materials were dissolved into 200 mL of Milli-Q Water, as illustrated in Table 1. Then, the beakers were stirred at 1000 rpm for 30 mins on a magnetic hotplate at room temperature to make homogenous solutions. Later, the NaOH solution was added drop wise under constant stirring (1000 rpm) until the mixture attained pH-10. Finally, the resultant precipitates were intensively washed 7 times using Milli-Q Water to remove the dissolved contaminants like sodium Na or Cl ions. The washed precipitates were dried at 80°C for 6 hrs and then calcined at 500°C for 3 hrs under atmospheric air with increasing rate of 5 C min^{-1}. The obtained powders of the pure, Fe-Cu, and Fe-V co-doped Mn_3O_4 nanoparticles were analyzed using different techniques.

2.2. Physical characterization and applied measurements

Purity, crystalline nature, and phases of the synthesized pure, Fe-Cu, and Fe-V co-doped Mn_3O_4 nanoparticles were examined through the Bruker D8 Advance XRD apparatus using cooper K-alpha radiation (λ = 1.5406 Å). The particle shape of pure, Fe-Cu, and Fe-V substituted Mn_3O_4 nanoparticles was studied by an HR-TEM (JEOL, JEM-100). The valence states of Mn, O, Fe, Cu, and V constituents were investigated by XPS (Al K-alpha radiation, Fisher Scientific, USA). The room temperature magnetic performance of pure, Fe-Cu, and Fe-V co-doped Mn_3O_4 samples was detected using a LakeShore 7410 vibrating sample magnetometer. The optical characteristics of pure, Fe-Cu, and Fe-V co-doped Mn_3O_4 samples were recorded by a DR tool (Shimadzu UV-2050).

Table 1. Required amounts of the chemical source materials (g) applied to synthesis pure, Fe-Cu, and Fe-V co-doped Mn_3O_4 nanoparticles.

Composition	$MnCl_2 \cdot 4H_2O$	$Cu(NO_3)_2 \cdot 3H_2O$	$Fe(NO_3)_2 \cdot 9H_2O$	NH_4VO_3
Mn_3O_4	9.896	-	-	-
2.5% Fe-2.5% Cu-Mn_3O_4	9.4	0.302	0.505	-
2.5% Fe-2.5% V-Mn_3O_4	9.4	-	0.505	0.146

The light-activated removal properties of pure, Fe-Cu, and Fe-V co-doped Mn_3O_4 photocatalysts for 25 mg/L Congo red (CR) dye were studied using the natural sunlight as a radiation source. The role of photolysis process (self-degradation) and the adsorption on the surface of the particles were measured and discussed. The main measurement of the photocatalytic performance was done by adding 0.06 g of pure, Fe-Cu, and Fe-V co-doped Mn_3O_4 nanoparticles to 100 mL solution containing dye concentration of 25 mg/L. The solutions of dye containing catalyst particles were irradiated for definite times under continuous stirring. The absorbance of the irradiated solutions was measured at fixed intervals to estimate the degradation value based on the relation (Eq. 1) [45]:

$$\text{Decolorization}(\%) = \frac{A_0 - A_t}{A_0} \times 100 \quad (1)$$

In relation (1), A_0 and A_t codes specify the initial concentration of CR dye solution (25 mg/L) and the concentration of irradiated solution for the CR contaminant.

3. Results and Discussion

3.1. XRD analysis

The crystallinity phase of pure, Fe-Cu, and Fe-V co-doped Mn_3O_4 nanoparticles synthesized via the coprecipitation route was well-identified using the XRD technique, as represented in Figure 1. As clarified in the XRD pattern of pure Mn_3O_4 powder, the characteristic peaks of (101), (112), (200), (103), (211), (004), (220), (105), (312), (303), (321), (224), (400), (305), (413), (422), and (404) planes were evidently matched to tetragonal structure of manganese (II,III) oxide, Mn_3O_4, (hausmannite, I41/amd, JCPDS file No. 80-0382) with calculated lattice constant “a” = “b” = 5.7734 Å and “c” = 9.4257 Å. The appearance of the same characteristics, crystallographic lines in the XRD patterns of Fe-Cu and Fe-V co-doped Mn_3O_4 samples confirmed the production of hausmannite structure with tetragonal phase. The high XRD intensity of the Fe-Cu co-doped Mn_3O_4 sample reflects the enhanced crystallinity, while the broadening of peaks of both co-doped samples can be related to the crystallite size reduction. No additional XRD peaks were observed in XRD patterns of pure and Fe-Cu and Fe-V co-doped samples, demonstrating the absence of impurities or any other phases of manganese oxides. Moreover, the Debye–Scherrer method, as given in Eq. (2), was applied to measure the average crystallite size (L) of pure, Fe-Cu, and Fe-V-modified Mn_3O_4 nanoparticles [46].

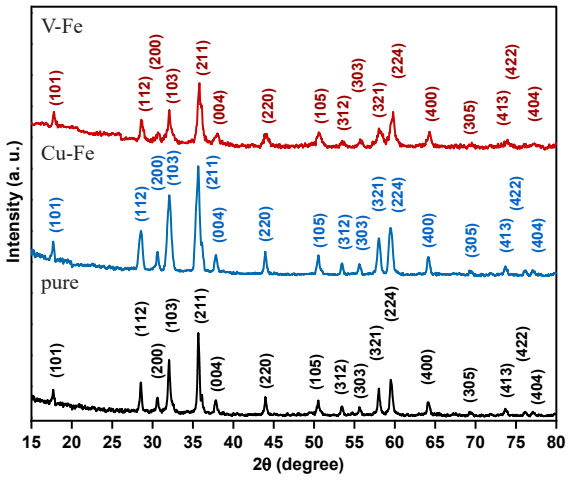

Figure 1. XRD patterns of pure, Cu-Fe, and V-Fe co-doped Mn_3O_4 nanoparticles.

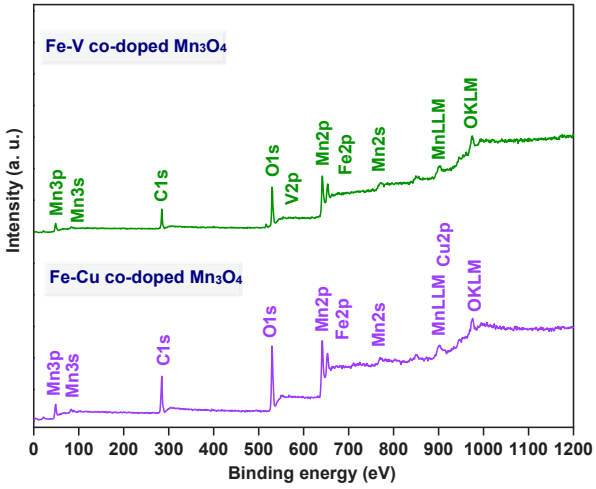

Figure 2. XPS survey spectra of Fe-V and Fe-Cu co-doped Mn_3O_4 compositions.

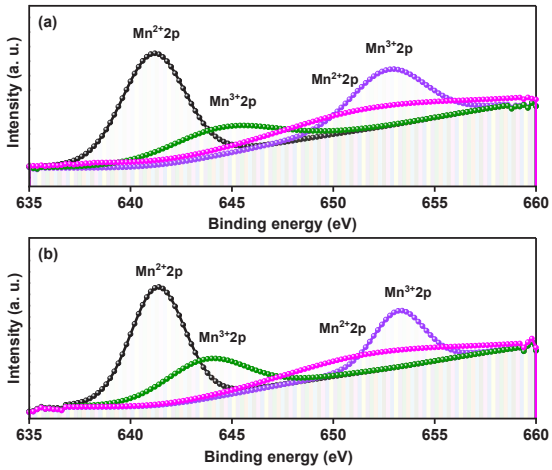

Figure 3. XPS of Mn 2p for (a) Fe-Cu co-doped Mn_3O_4 and (b) Fe-V co-doped Mn_3O_4 compositions.

$$L = \frac{0.9\lambda}{\beta \cos\theta} \quad (2)$$

The θ value in the Debye–Scherrer equation indicates the angle of the XRD peaks, β reflects the full width at half maximum and λ signifies the wavelength of the copper alpha radiation (1.5406 Å). For pure, Fe-Cu, and Fe-V-modified Mn_3O_4 nanoparticles, the average crystallite sizes were computed based on three main XRD peaks for each sample to be 50, 22, and 31 nm, respectively.

3.2. XPS

Figure 2 depicts the XPS survey spectra of Fe-Cu and Fe-V co-doped Mn_3O_4 samples, illuminating the occurrence of carbon (C), manganese (Mn), oxygen (O), iron (Fe), copper (Cu) and vanadium (V) elements. The nonappearance of any other elements point to the purity of the Fe-Cu and Fe-V co-doped Mn_3O_4 compositions. Figure 3 represents the high-resolution deconvoluted XPS spectra of the Mn2p state, where binary twofold binding energy peaks were identified as Mn $2p_{1/2}$ and Mn $2p_{3/2}$. Based on the XPS spectra of Mn 2p for Fe-Cu-modified Mn_3O_4 composition, the two valence states are distinguished as Mn^{2+} (641.15 and 652.09 eV) and Mn^{3+} state (644.45 and 652.94 eV). For the Fe-V co-doped Mn_3O_4 sample, the deconvoluted core level spectrum of Mn 2p gives binding energy peaks at 641.35 and 652.11 eV related to the Mn^{2+} state, while the binding energies at 643.74 and 653.24 were linked to the Mn^{3+} state [47-49]. As given in Figure 4, the XPS of O 1s for Fe-Cu co-doped Mn_3O_4 composition reveals three different deconvolution signals at binding energies equal to 528.97, 530.05, and 531.42 eV, which are indexed to lattice oxygen, oxygen vacancy, and chemisorbed oxygen, respectively [50]. The deconvoluted core level splitting pattern of O 1s for Fe-V co-doped Mn_3O_4 powder displays binding energy peaks at 530.04, 531.54 and 532.69 eV, which also attributed to lattice oxygen, oxygen vacancy, and chemisorbed oxygen species, respectively [50]. The XPS signals of the O 1s state verified the presence of oxygen vacancy defects in both co-doped Mn_3O_4 compositions.

Figure 5 gives the high-resolution deconvoluted core-level splitting patterns of Fe, Cu, and V dopants used to modify the Mn_3O_4 structure.

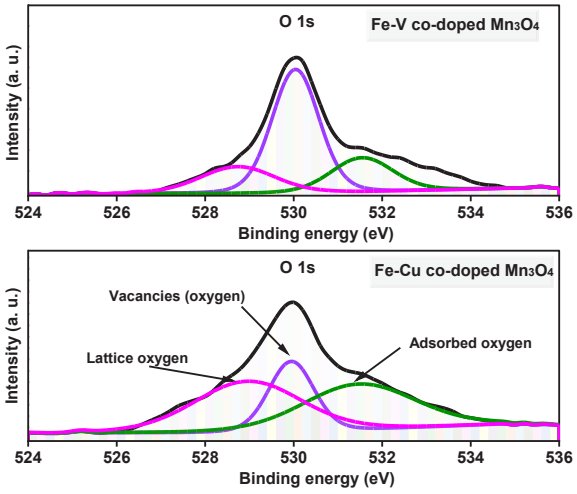

Figure 4. XPS of O 1s for Fe-V and Fe-Cu co-doped Mn_3O_4 compositions.

The pattern of the XPS spectrum of the magnetic Fe ions of Fe-Cu co-doped Mn_3O_4 structure displays that the divalent Fe^{2+} and the trivalent Fe^{3+} ions are present in this composition [51,52]. The binding energy peaks located at 709.16, 713.65 (satellite), and 722.99 eV are in agreement with the XPS analysis of Fe^{2+}-2p, while the binding energy peaks situated at 711.29, 718.22 (satellite), and 725.37 eV were related to Fe^{3+}-2p XPS data. As noticed in Figure 5(a), the nonappearance of a peak around 706-707 eV rules out the occurrence of metallic iron (Fe) element in Fe-Cu co-doped Mn_3O_4 composition. In Figure 5(b), the high-resolution deconvoluted core level splitting of Cu^{2+} XPS approves the doping of Cu^{2+} ions by revealing two binding energy peaks at 933.79 eV and a satellite peak at 944.43 eV of Cu 2p state [48]. As shown in Figure 5(c), the high-resolution deconvoluted spectrum of V dopant gives a peak located at 516.71 eV, which indicates the presence of V^{4+}

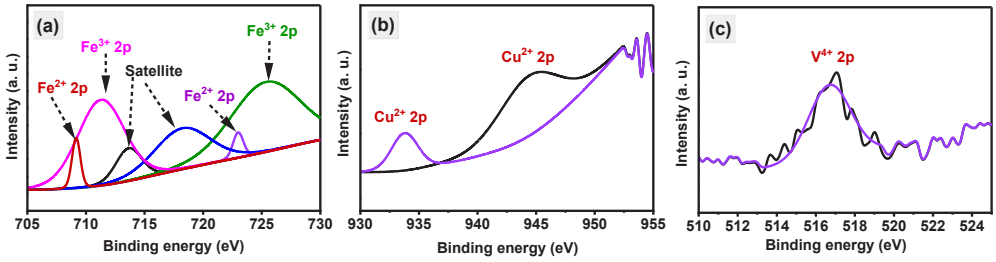

Figure 5. Deconvoluted core-level splitting patterns of (a) Fe, (b) Cu and (c) V dopants used to modify Mn_3O_4 nanoparticles.

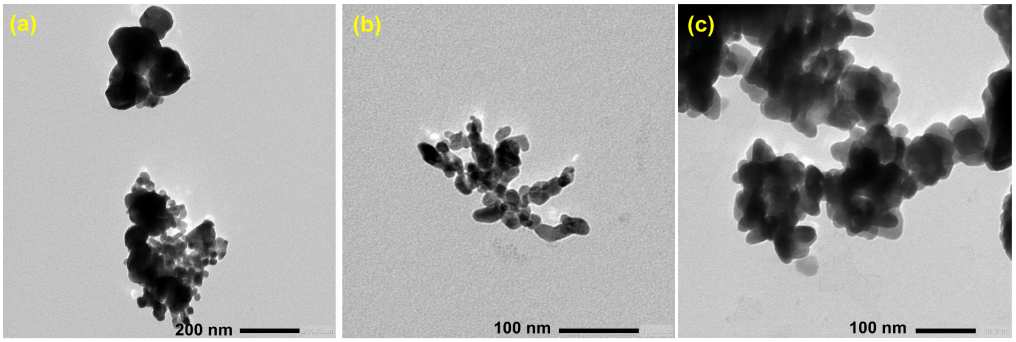

Figure 6. Images of TEM analysis of (a) pure, (b) Fe-Cu, and (c) Fe-V incorporated Mn_3O_4 structure.

oxidation state inside the Fe-V co-doped Mn_3O_4 sample [53]. These results verify that the dopants of Fe, Cu, and V ions hold the +2/+3, +2 and +4 oxidation states without the presence of any metallic forms in these constituents, respectively. The absence of any metallic form of Fe dopant ruled out its effect on the magnetic properties of Mn_3O_4 sample. Besides, the electronic configurations of Fe^{2+}, Fe^{3+}, Cu^{2+}, and V^{4+} ions are [Ar] $3d^6$, [Ar] $3d^5$, [Ar] $3d^9$, and [Ar] $3d^1$, respectively. The presence of unpaired electrons in the 3d-orbitals of these dopants, besides the existence of oxygen vacancies, can greatly improve the magnetic properties of the Mn_3O_4 sample.

3.3. TEM

The detailed morphological particles size and shape of pure, Fe-Cu, and Fe-V co-doped Mn_3O_4 powders were analyzed by a TEM device, as presented Figure 6. The details from the TEM image of the pure Mn_3O_4 sample illustrate the formation of agglomerated particles with an irregular shape and an average size of 46 nm. As noticed in the TEM image of Fe-Cu co-doped Mn_3O_4 powder, quasi-spherical homogenous particles formed with an average size of 19 nm, Figure 6(b). The morphological TEM image of Fe-V incorporated into Mn_3O_4 powder displayed the manufacture of uniform particles with an average size of 35 nm and a high agglomeration ratio.

3.4. DR study

Figure 7 displays the pattern of DR analysis of pure, Cu-Fe, and V-Fe modified Mn_3O_4 nanoparticles in the spectral area from 200 to 2400 nm, which is parallel to UV, visible light, and IR regions. The curves of the samples give obvious absorption band edges at different wavelengths, indicating the dissimilarity in the band gap energies. As seen in Figure 7, the absorption band edge of pure Mn_3O_4 compound was moved to a lower energy region due to the introducing of Cu-Fe and V-Fe ions into the host lattices, besides the observed decreases in the reflectance intensity. The assessment of the band gap energy values of pure, Cu-Fe, and V-Fe modified Mn_3O_4 nanoparticles can be calculated accurately by using the Kubelka-Munk (Eq. 3) [54]:

$$[F(R_\infty)h\nu]^n = A(h\nu - E_g) \quad (3)$$

In Eq. (3), hv is the energy of the incident photon, F(R) is the Kubelka-Munk function, E_g stands for the band gap energy, and A is a proportional constant. In this formula, "n" was considered as 2

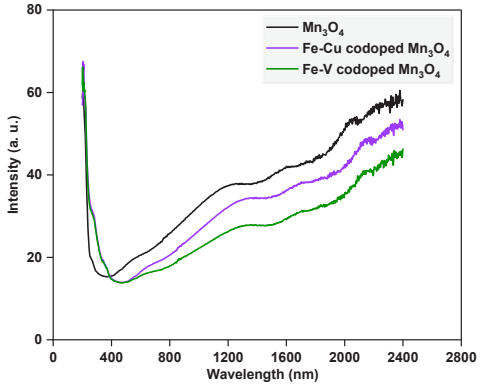

Figure 7. DR spectra of pure, Cu-Fe, and V-Fe co-doped Mn_3O_4 nanoparticles.

for a direct transition and 1/2 for an indirect transition. As well, the Kubelka–Munk function can be expressed by formula (Eq. 4) [54]:

$$F(R_\infty) = \frac{(1-R)^2}{2R} = \frac{K}{S} \quad (4)$$

Where S, K, and R indicate the scattering coefficient, absorption coefficient, and reflection coefficient, respectively. As illustrated in Figure 8, ($[F(R)hv]^2$ vs. hv), from the linear extrapolation of $[F(R)hv]^2$ to zero point, the band gap energy values of pure, Cu-Fe, and V-Fe modified Mn_3O_4 nanoparticles were estimated to be 2.1, 1.78, and 1.65 eV, respectively. The band gap of the prepared Mn_3O_4 nanoparticles is in agreement with published values [55-57]. The introducing of impurity levels by Cu-Fe and V-Fe ions reduces the band gap energy of pure Mn_3O_4 nanoparticles and gives obvious signs to the active substitution process.

3.5. Room temperature magnetic analysis

To study the influence of Cu-Fe and V-Fe ions on the magnetic order of Mn_3O_4 nanoparticles, the vibrating sample magnetometer analysis was carried out at room temperature. Figure 9 displays the applied magnetic field dependent magnetization (M–H curves) of pure, Fe-Cu, and Fe-V co-doped Mn_3O_4 nanoparticles at room temperature (300 K).

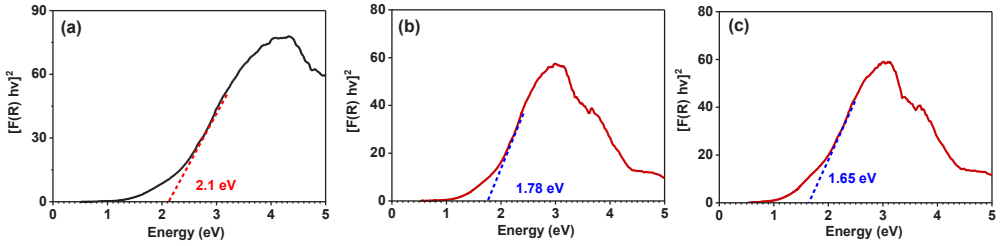

Figure 8. Band gap energy of (a) pure, (b) Fe-Cu, and (c) Fe-V co-doped Mn_3O_4 nanoparticles.

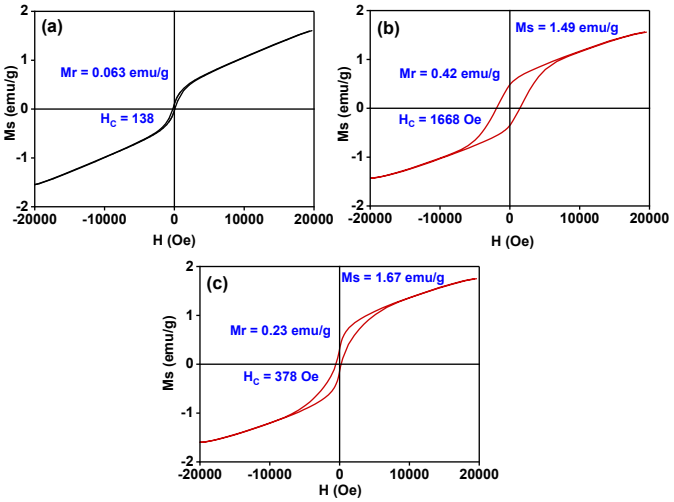

Figure 9. Room temperature magnetic properties of (a) pure, (b) Fe-Cu, and (c) Fe-V co-doped Mn_3O_4 nanoparticles.

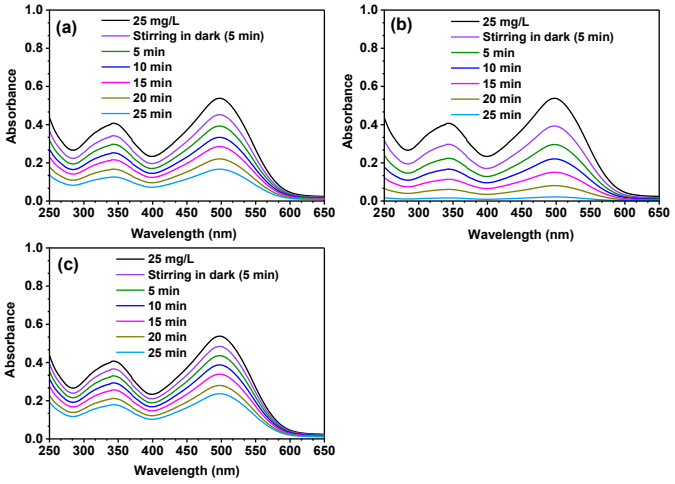

Figure 10. The absorbance spectra depicting degradation of CR dye under solar light at room temperature for (a) pure, (b) Fe-Cu, and (c) Fe-V co-doped Mn_3O_4 nanoparticles.

As shown in Figure 9(a), the M–H plot of pure Mn_3O_4 nanoparticles shows semi-linear performance with a narrow and weak hysteresis loop within ±1000 Oe, indicating the presence of general paramagnetic performance with very weak ferromagnetic order at low magnetic field. The measured coercivity and remanence (retentivity) values from the hysteresis part of the curve of pure Mn_3O_4 nanoparticles were 138 Oe and 0.063 emu/g. However, the M–H plots of Fe-Cu and Fe-V co-doped Mn_3O_4 nanoparticles exhibit markedly different magnetization loops compared to pure Mn_3O_4 nanoparticles. Clearly, Fe-Cu and Fe-V modified Mn_3O_4 nanoparticles revealed room temperature ferromagnetism with characterized hysteresis shape. As demonstrated in Figure 9(b), the magnetic curve of Fe-Cu co-doped Mn_3O_4 powder gives high coercivity and remanence (retentivity) values of 1668 Oe and 0.42 emu/g with measured saturation magnetization equal to 1.49 emu/g, respectively. In the same direction, the hysteresis curve of Fe-V co-doped Mn_3O_4 semiconductor exhibits coercivity, remanence, and saturation magnetization values of 378 Oe, 0.23 emu/g, and 1.67 emu/g, respectively. At room temperature, the pure Mn_3O_4 powder displayed a paramagnetic, with weak hysteresis at low field, which is in agreement with the previous published reports [12,54]. The detected high saturation magnetization and coercivity values of Fe-Cu and Fe-V modified Mn_3O_4 nanoparticles are an important issue, which highlight the potential appropriateness of co-doped Mn_3O_4 nanoparticles for use in magnetic data storage, MRI, biomedical imaging and drug delivery [12,58].

Nevertheless, the origin of room temperature ferromagnetism can include a very complex process. At present, there is no agreement on the origin of room temperature ferromagnetism in doped oxide materials, although many theoretical concepts have been suggested to explain this ferromagnetic ordering [12,58]. The model of the free-carrier-mediated ferromagnetism was suggested to clarify the magnetic characteristics of Mn-doped III-V semiconductors. However, room temperature ferromagnetism based on the model of the free-carrier predicted for Mn-doped III-V semiconductors may not be appropriate to Mn_3O_4, as it is highly resistive. Also, the presence of small Fe, Cu, and V clusters or any second phases was ruled out since the characterization analysis of XRD, DR, and XPS did not give any sign for these constituents. The XPS results confirmed that the Fe, Cu, and V ions present as +3/+2, +2, and +4 oxidation states without any metallic form, respectively. The XPS analysis recommends that the $Fe^{2+/3+}$, Cu^{2+}, and V^{4+} ions replace the Mn sites in the Mn_3O_4 lattice. The presence of oxygen vacancies inside Fe-Cu and Fe-V co-doped Mn_3O_4 nanoparticles was verified based on XPS patterns of the O 1s orbital. As a result, according to our organized characterization analyses, the oxygen vacancies mediated bound magnetic polarons (BMPs) exchange interaction can be recommended for the origin of room temperature ferromagnetism in these compositions [58]. The oxygen vacancies inside Fe-Cu and Fe-V modified Mn_3O_4 nanoparticles can actively align with the $Fe^{2+/3+}$, Cu^{2+}, and V^{4+} cations, leading to operative hybridization for dopants and defects, which can induce room temperature ferromagnetic order in Fe-Cu and Fe-V co-doped Mn_3O_4 nanoparticles. The exchange interaction between the $Fe^{2+/3+}$, Cu^{2+}, and V^{4+} ions and the contamination band made by these defects (oxygen vacancies) proposes the construction of BMPs, which regulate the ferromagnetic ordering, leading to this improved room temperature ferromagnetic performance.

3.6. Photocatalytic study

The photocatalytic investigation of the obtained compositions was estimated by the photocatalytic elimination of CR (25 mg/L) in an aqueous solution under ordinary solar irradiation. The 25 mg/L CR dye solutions (100 mL) were readied from the stock solution of CR pollutant, and 0.6 g of pure, Fe-Cu, and Fe-V modified Mn_3O_4 catalysts were suspended. The obtained solutions were stirred for 5 mins in a dark environment before being exposed to solar radiation. At ordered time intervals (5 mins), ~ 3–4 mL of dark and irradiated solution were taken out using a 10 mL syringe, and the particles of the pure, Fe/Cu, and Fe/V modified Mn_3O_4 catalysts were separated through a centrifuge device. The absorbance opposed to wavelength (λ, nm) of the photodegraded CR samples was measured from 250 to 650 nm via using UV-visible spectrophotometer, as revealed in Figure 10. The absorbance peak at 497 nm was utilized to calculate the concentration value of organic CR pollutant for each interval time (5 mins). Primarily, pure, Fe-Cu, and Fe-V modified Mn_3O_4 semiconductor catalysts had adsorption values of CR dye of 16, 27, and 11%, respectively. Also, the photolysis process of CR dye in the absence of the catalyst ruled out the self-degradation under sunlight irradiation. After 25 mins of solar irradiation, the photocatalytic process was completed for the Fe-Cu modified Mn_3O_4 catalyst. Exactly, the absorbance vs. wavelength plot of the CR solution using pure Mn_3O_4 semiconductor catalyst reflects a degradation efficiency of 59% after 25 mins. For the Fe-Cu modified Mn_3O_4 catalyst, the changes in the absorbance peak at 497 nm confirmed a photo-removal activity of 98% during 25 mins of solar light irradiation. On contrast, the variations of absorbance peak at 497 nm of CR solution using Fe-V modified Mn_3O_4 semiconductor catalyst provides a photodegradation activity of 56% in the same period. The sequence of degradation efficiency was Fe-Cu modified Mn_3O_4 > Mn_3O_4, > Fe-V modified Mn_3O_4 catalysts. The results clarify that the addition of Fe-Cu ions remarkably trigger the photo-removal efficiency of Mn_3O_4 semiconductor towards CR dye, while the Fe-V blend slightly weak the activity.

Two of the main factors that influence the degradation activity of the photocatalytic process are the broad absorption of light energy (photons) and the effective separation of charge carriers. Both co-doped samples have broad absorption properties, but it seems that the addition of Fe-Cu supports the charge carriers' separation, which

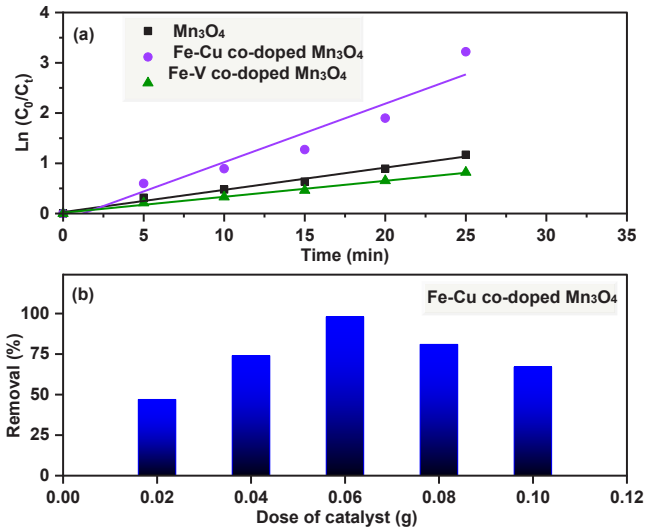

Figure 11. Shows (a) Kinetic plots of photodegradation of CR dye under solar light for pure, Fe-Cu, and Fe-V co-doped Mn_3O_4 nanoparticles and (b) impact of dose of Fe-Cu co-doped Mn_3O_4 catalyst on removal efficiency for CR dye.

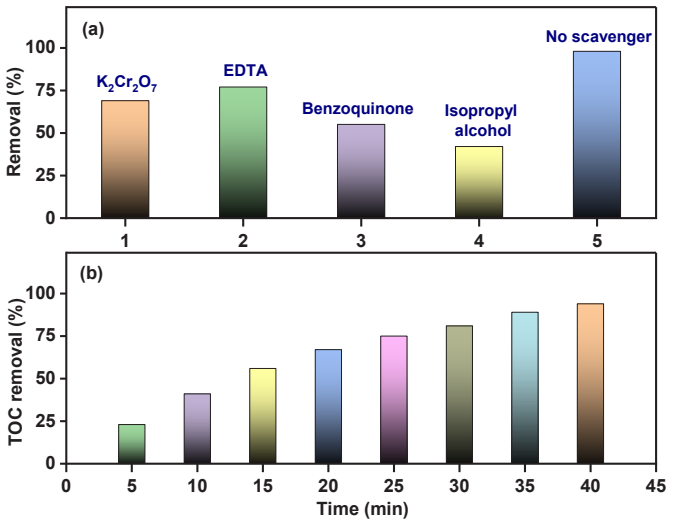

Figure 12. Illustrates (a) effect of chemical scavengers on degradation efficiency of Fe-Cu co-doped Mn_3O_4 catalyst and (b) TOC removal (%) test of Fe-Cu co-doped Mn_3O_4 catalyst for analysis of CR mineralization. EDTA: Ethylenediamine tetraacetic acid.

limits their recombination. The presence of V^{4+} ions seems to increase the recombination rate of the charge carriers. Furthermore, the TEM images confirmed that Fe-Cu modified Mn_3O_4 catalysts have the smallest particle sizes, which can increase the reaction surface.

As displayed in Figure 11(a), the plots of $\ln(C_0/C_t)$ vs. time of irradiation represent the kinetic performance for the elimination of CR dye by the prepared pure, Fe-Cu, and Fe-V modified Mn_3O_4 catalysts. The kinetics of photodegradation reaction of pure, Fe-Cu and Fe-V modified Mn_3O_4 catalysts has been analyzed by using the well-known pseudo-first-order kinetic formula using Langmuir-Hinshelwood (LH) model, as shown in (Eq. 5) [59]:

$$ln\frac{C_0}{C_t} = k_{app}t \tag{5}$$

In this formula, "k_{app}" stands for the apparent rate constant of Langmuir-Hinshelwood first-order model, "t" represents the time of each interval, C_0 is the main concentration, and C_t is the concentration of degraded solutions at different interval times. The values of apparent rate constant (k_{app}) were calculated by linear fit of points of $\ln(C_0/C_t)$ vs. time (min) plots. The achieved values of apparent rate constant (k_{app}) for pure, Fe-Cu, and Fe-V modified Mn_3O_4 catalysts are ~ 0.044, 0.12 and 0.03 min^{-1}, respectively. The photodegradation first-order apparent rate constant (k_{app}) of Fe-Cu modified Mn_3O_4 catalyst is higher than that of Mn_3O_4 and Fe-V modified Mn_3O_4 catalysts. Moreover, the best catalyst dose of Fe-Cu modified Mn_3O_4 sample for photo-removal of CR dye has also been identified by varying the photocatalyst quantity from 0.02 to 0.1 g under solar irradiation with a fixed CR concentration of 25 mg/L, and the achieved photodegradation efficiencies were graphically plotted in Figure 11(b). As noticed in Figure 11(b), the photo-removal of CR dye was intensely affected by the dose of Fe-Cu modified Mn_3O_4 catalyst. 47% photodegradation efficiency of CR dye was detected when 0.02 g of Fe-Cu modified Mn_3O_4 catalyst was used. When the amount of Fe-Cu modified Mn_3O_4 catalyst was increased to 0.04, 0.06, 0.08, and 0.1 g, 74%, 98%, 81%, and 67% degradation efficiencies of CR dye were recorded, respectively. It is noticeable that by increasing the Fe-Cu modified Mn_3O_4 catalyst from 0.02 g to 0.06 g, the photo-removal efficiency of CR dye was improved from 47% to 98% under the same conditions. These improvements can be seemingly attributed to the availability of more energetic sites that can yield extra reactive radicals by increasing the Fe-Cu modified Mn_3O_4 photocatalyst. But the further growth of Fe-Cu modified Mn_3O_4 catalyst may increase the opaqueness of the solution, leading to the hindering of solar light penetration, which reduces the activity of the removal of CR dye. As a result, the suitable amount of Fe-Cu modified Mn_3O_4 photocatalyst was estimated to be 0.06 g.

The superoxide ($O_2^{\cdot-}$) and hydroxyl ions (·OH) radicals are highly energetic and non-stable reactive species that commonly possess a remarkable influence on the photo-removal of organic pollutants such as dyes. To know the roles of the superoxide ($O_2^{\cdot-}$), hydroxyl (·OH) ions, holes or negative electrons species on the activity of Fe-Cu modified Mn_3O_4 photocatalyst for decomposition of CR dye, different chemical trapping agents were added. Herein, the $K_2Cr_2O_7$ was used to capture electrons, isopropyl alcohol to attack ·OH, EDTA to detect the positive holes and benzoquinone to identify the superoxide ($O_2^{\cdot-}$). As illustrated in Figure 12(a), the activity of the degradation of Fe-Cu co-doped Mn_3O_4 photocatalyst for CR dye was noticeably dropped after using the isopropyl alcohol and benzoquinone scavengers which indicate that the hydroxyl (·OH) and superoxide ($O_2^{\cdot-}$) radicals are the power species to remove this dye using Fe-Cu co-doped Mn_3O_4 photocatalyst.

To examine the real applicability of Fe-Cu co-doped Mn_3O_4 photocatalyst, the total organic carbon (TOC) was calculated based on the relation (Eq. 6) [60]:

$$\%TOC = \frac{TOC_0 - TOC_t}{TOC_0} \times 100 \tag{6}$$

In relation (6), TOC_0 and TOC_t represent the primary TOC and their values at different solar irradiation, respectively. As illustrated in Figure 12(b), the % TOC elimination of Fe-Cu cdoped Mn_3O_4 photocatalyst is 94.5% for 25 mg/L CR dye, demonstrating that the major hazardous and non-hazardous by-products were converted (mineralized) into H_2O and CO_2 after 40 min, which confirms the perfect mineralization for CR dye. The mineralization process takes more time compared to the decolorization of CR dye. This difference can be related to the production of intermediate products during the mineralization process, and finally, these compounds are converted to H_2O and CO_2 molecules.

The photodegradation reusability of the Fe-Cu modified Mn_3O_4 photocatalyst was examined under similar treatment conditions. The recycled photodegradation processes were symbolized as 1R, 2R, 3R, and 4R, indicating the first, second, third, and fourth cycles, respectively. The reusability test is used to explore the stability of the Fe-Cu modified Mn_3O_4 photocatalyst for the green environmental remediation process. As shown in Figure 13, the Fe-Cu modified Mn_3O_4 photocatalyst revealed good reusability and stability properties until the fourth cycle. The measured photodegradation efficiencies of Fe-Cu modified Mn_3O_4 photocatalyst for 1R, 2R, 3R, and 4R cycles were 98%, 93%, 86%, and 79%, respectively. The decreases in the photocatalytic efficiency of Fe-Cu co-doped Mn_3O_4 photocatalyst may be ascribed to the amount of catalyst lost during the washing and drying processes for each cycle. These findings recommend that Fe-Cu co-doped Mn_3O_4 photocatalyst has the potential to be utilized for a long time in the degradation reaction of CR dye.

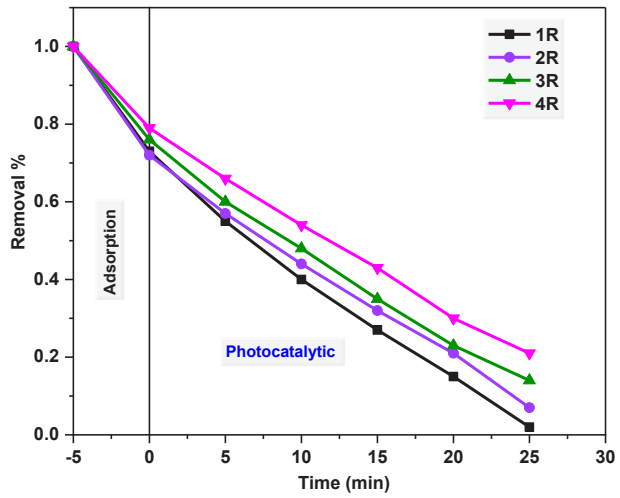

Figure 13. Stability and reusability test of Fe-Cu co-doped Mn_3O_4 catalyst towards CR pollutant.

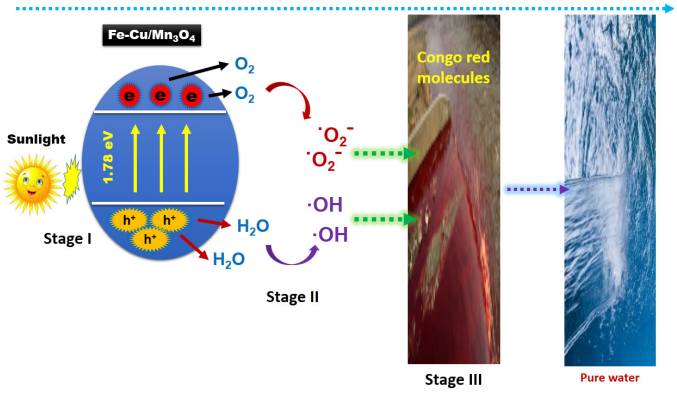

Figure 14. Diagram depicting a proposed mechanism of CR degradation using Fe-Cu co-doped Mn_3O_4 catalyst.

Commonly, the photodegradation of organic dyes, pharmaceutical compounds, or other contaminants by oxides semiconductor photocatalysts includes three stage of reactions; (I): producing of negative electron (e-) and positive holes (h^+) at the conduction band (CB) and valence band (VB) of Fe-Cu modified Mn_3O_4 photocatalyst under solar irradiation, respectively; (II): the produced e- and h^+ transfer to the surface of Fe-Cu co-doped Mn_3O_4 particles and react with oxygen (O_2) and water (H_2O) to produce other superoxide ($O_2^{\cdot-}$), and hydroxyl (·OH) reactive species; and finally (III): the superoxide ($O_2^{\cdot-}$), and hydroxyl (·OH) reactive species attack and degrade CR molecules via robust oxidation and reduction reactions, as illustrated in Figure 14 and clarified in the following steps (Eq. 7) [61-63]:

$$
\begin{aligned}
&Cu\,/\,Fe-Mn_3O_4 \rightarrow \text{Photons} \rightarrow e^- + h^+\\
&e^- + O_2 \rightarrow O^{\cdot-}\\
&h^+ + H_2O \rightarrow OH^{\cdot} + H^+\\
&h^+ + OH^- \rightarrow OH^{\cdot}\\
&Cu^{2+} + e^- \rightarrow Cu^+\\
&Fe^{3+} + e^- \rightarrow Fe^{2+}\\
&Cu^+ \text{or } Fe^{2+} + O_2 \rightarrow Cu^{2+} + Fe^{3+} + O^{\cdot-}\\
&O^{\cdot-} \,/\, OH^{\cdot} + \text{CR moleclues} \rightarrow H_2O + CO_2
\end{aligned}
\tag{7}
$$

4. Conclusions

The discharge of industrial organic contaminants such as colored dyes into surface water has a dangerous influence on the environment and all living organisms. Thus, the efficient and fast treatment of these dissolved pollutants is an important issue. In this study, new Fe-Cu and Fe-V co-doped Mn_3O_4 compositions were synthesized for the active treatment of wastewater. The obtained results revealed that the Fe-Cu and Fe-V co-doped Mn_3O_4 compositions have strong ferromagnetic behavior and superior catalytic properties for technological and environmental applications. The XPS signals of Fe-Cu and Fe-V co-doped Mn_3O_4 compositions confirmed the valence states of +2/+3, +3, and +4 for Cu, Fe, and V dopants inside Mn_3O_4 structure, respectively. The intrinsic ferromagnetism of Fe-Cu and Fe-V co-doped Mn_3O_4 compositions at room temperature was related to Cu^{2+}, $Fe^{2+/3+}$, and V^{4+} dopants as well as defects (oxygen vacancies). The saturation magnetization of 1.49 and 1.67 emu/g, as well as coercivity of 1668 and 378 Oe, were detected for Fe-Cu and Fe-V co-doped Mn_3O_4 compositions, respectively. The detected ferromagnetism performance was modeled by the BMPs' mechanism. The perfect photo-removal efficiency of Fe-Cu co-doped Mn_3O_4 catalyst was verified for CR dye with a maximum activity of 98% after of 25 mins of sunlight irradiation. As a result, the Fe-Cu co-doped Mn_3O_4 composition is a really promising catalyst, which needs to be industrialized for green environmental uses.

CRediT authorship contribution statement

This study was completely prepared by Dr. Ghayah M Alsulaim.

Declaration of competing interest

All the authors declare no competing interests.

Declaration of Generative AI and AI-assisted technologies in the writing process

The authors confirm that there was no use of artificial intelligence (AI)-assisted technology for assisting in the writing or editing of the manuscript and no images were manipulated using AI.

Acknowledgment

This work was supported by the Deanship of Scientific Research Vice Presidency for Graduate Studies and Scientific Research, King Faisal University, Saudi Arabia [project Number: KFU251301].

References

1. Prasad, K., Sreekanth, T.V.M., Yoo, K., Kim, J., 2024. Facile synthesis of Mn_3O_4 nanoparticles towards high performance asymmetric supercapacitors. *Vacuum*, **221**, 112930. https://doi.org/10.1016/j.vacuum.2023.112930
2. Horti, N.C., Samage, A., Halakarni, M.A., Chavan, S.K., Inamdar, S.R., Kamatagi, M.D., Nataraj, S.K., 2024. Optical and electrochemical properties of manganese oxide (Mn_3O_4) nanoparticles: Investigating the influence of calcination temperature on supercapacitor performance. *Materials Chemistry and Physics*, **318**, 129276. https://doi.org/10.1016/j.matchemphys.2024.129276
3. Godlaveeti, S.K., Shuailiang, X., Weng, H., Mingqiang, L., Ying, H., 2025. Unlocking enhanced new type of safe open system lithium-ion battery performance: Mn_3O_4 nano-cubes and their sulfur mixers cathode material. *Journal of Molecular Structure*, **1319**, 139563. https://doi.org/10.1016/j.molstruc.2024.139563
4. Zhu, L., Zhang, W., Chen, J., Men, L., Zhang, J., Zhou, Y., 2024. Deciphering the storage mechanism of biochar anchored with different morphology Mn_3O_4 as advanced anode material for lithium-ion batteries. *Journal of Colloid and Interface Science*, **669**, 740-753. https://doi.org/10.1016/j.jcis.2024.05.044
5. Khan, S., Hussain, A., He, K., Liu, B., Imran, Z., Ambreen, J., Hassan, S., Ahmad, M., Batool, S.S., Li, C., 2021. Tailoring the bandgap of Mn_3O_4 for visible light driven photocatalysis. *Journal of Environmental Management*, **293**, 112854. https://doi.org/10.1016/j.jenvman.2021.112854
6. Gupta, A., Kajal, , Ajravat, K., Brar, L.K., Pandey, O.P., Rajagopalan, P., 2024. Facile synthesis of Mn_3O_4–ZnO composite for photocatalytic dye removal and capacitive applications. *Materials Chemistry and Physics*, **313**, 128698. https://doi.org/10.1016/j.matchemphys.2023.128698
7. Hasan, G.G., Laouini, S.E., Osman, A.I., Bouafia, A., Althamthami, M., Meneceur, S., Al-Hazeef, M.S.F., Al-Fatesh, A.S., Rooney, D.W., 2024. Green synthesis of Mn_3O_4@CoO nanocomposites using Rosmarinus officinalis L. extract for enhanced photocatalytic hydrogen production and CO_2 conversion. *Journal of Environmental Chemical Engineering*, **12**, 113911. https://doi.org/10.1016/j.jece.2024.113911
8. Tseng, Z.-C., Jiang, Y.-Y., Lin, C.-Y., Do, J.-Y., Hsu, T.-H., Shih, C.-W., Chang, Y.-Z., Liao, S.-Y., Huang, C.-Y., 2024. Highly stable flexible ozone gas sensors using Mn_3O_4

nanoparticles-decorated IGZO thin films through the SILAR method. *Ceramics International*, **50**, 28584-28592. https://doi.org/10.1016/j.ceramint.2024.05.168
9. Kortidis, I., Swart, H.C., Ray, S.S., Motaung, D.E., 2019. Characteristics of point defects on the room temperature ferromagnetic and highly NO_2 selectivity gas sensing of p-type Mn3O4 nanorods. *Sensors and Actuators B: Chemical*, **285**, 92-107. https://doi.org/10.1016/j.snb.2019.01.007
10. Feng, X., Zhai, B., Cheng, R., Yin, L., Wen, Y., Jiang, J., Wang, H., Li, Z., Zhu, Y., He, J., 2023. Phase Engineering of 2D Spinel-Type Manganese Oxides. *Advanced Materials (Deerfield Beach, Fla.)*, **35**, e2304118. https://doi.org/10.1002/adma.202304118
11. Liu, Y., Shi, Y., Feng, Q., Chen, M., Cao, D., 2018. Distribution-dependent capacitive and magnetic properties of Mn_3O_4 nanoparticles on reduced graphene oxide. *Diamond and Related Materials*, **84**, 169-177. https://doi.org/10.1016/j.diamond.2018.03.024
12. Li, G.M.in, Tang, X.B.ing, Lou, S.Y.un, Zhou, S.M.in, 2014. Large enhancement of ferromagnetism by Cr doping in Mn_3O_4 nanowires. *Applied Physics Letters*, **104**. https://doi.org/10.1063/1.4874272
13. Li, K., Zhang, C., Li, X., Du, Y., Yang, P., Zhu, M., 2019. A nanostructured $CuWO_4$/Mn_3O_4 with p/n heterojunction as photoanode toward enhanced water oxidation. *Catalysis Today*, **335**, 173-179. https://doi.org/10.1016/j.cattod.2018.11.003
14. Şahin, B.ünyamin, Aydin, R., Cetin, H., 2020. Tuning the morphological, structural, optical and dielectric properties of hausmannite (Mn_3O_4) films by doping heavy metal lead. *Superlattices and Microstructures*, **143**, 106546. https://doi.org/10.1016/j.spmi.2020.106546
15. Pugazhvadivu, K.S., Ashokkumar, M., 2024. Tuning the optical and magnetic properties of Mn_3O_4 quantum dots by annealing process. *Journal of Materials Science: Materials in Electronics*, **35**, 830. https://doi.org/10.1007/s10854-024-12519-2
16. Pandey, V., Adiba, A., Munjal, S., Ahmad, T., 2020. Structural and magnetic properties of tetragonal Mn_3O_4 nanoparticles synthesized by sol-gel method. *AIP Conference Proceedings*, **2220**, 020163. https://doi.org/10.1063/5.0001796
17. Du, J., Gao, Y., Chai, L., Zou, G., Li, Y., Qian, Y., 2006. Hausmannite Mn_3O_4 nanorods: synthesis, characterization and magnetic properties. *Nanotechnology* 17, 4923. https://doi.org/10.1088/0957-4484/17/19/024
18. Ijaz Dar, G., Iqbal, M.Z., Akakuru, O.U., Yao, C., Awiaz, G., Wu, A., 2020. Facile synthesis of Au@Mn_3O_4 magneto-plasmonic nanoflowers for T1-weighted magnetic resonance imaging and photothermal therapy of cancer. *Journal of materials chemistry. B*, **8**, 8356-8367. https://doi.org/10.1039/d0tb01526a
19. Mandal, S., Baskey, M., Saha, S.K., 2013. A demonstration of half-metallicity in graphene using Mn_3O_4 nanosheet. *Carbon* **61**, 254–259. https://doi.org/10.1016/j.carbon.2013.05.002
20. Raja, G., Nallathambi, A., Prakasam, A., Gopinath, S., Ragupathi, C., Narayanan, S., Tamizhdurai, P., Kumaran, R., Alsaiari, N.S., Abualnaja, K.M., Ouladsmane, M., 2022. Effect of lattice strain on structure, morphology, electrical conductivity and magneto-optical and catalytic properties of Ni-doped Mn_3O_4 nano-crystallites synthesized by microwave route. *Journal of Saudi Chemical Society*, **26**, 101440. https://doi.org/10.1016/j.jscs.2022.101440
21. Kanwal, S., Khan, M.T., Mehboob, N., Amami, M., Zaman, A., 2022. Room-Temperature Ferromagnetism in Cu/Co Co-Doped ZnO Nanoparticles Prepared by the Co-Precipitation Method: For Spintronics Applications. *ACS omega*, **7**, 32184-32193. https://doi.org/10.1021/acsomega.2c03375
22. Li, Q., Yuan, H., Zhang, Y., Yan, W., Zhang, S., Liao, B., Ying, M., 2023. Enhanced room-temperature ferromagnetism in Co and Er co-implanted MgO film. *Materials Letters* **333**, 133646. https://doi.org/10.1016/j.matlet.2022.133646
23. Nazri, M.K.H.M., Sapawe, N., 2020. A short review on photocatalytic toward dye degradation. *Materials Today: Proceedings*, **31**, A42-A47. https://doi.org/10.1016/j.matpr.2020.10.967
24. Dihom, H.R., Al-Shaibani, M.M., Mohamed, R.M.S.R., Al-Gheethi, A.A., Sharma, A., Khamidun, M.H.B., 2022. Photocatalytic degradation of disperse azo dyes in textile wastewater using green zinc oxide nanoparticles synthesized in plant extract: A critical review. *Journal of Water Process Engineering*, **47**, 102705. https://doi.org/10.1016/j.jwpe.2022.102705
25. Iqbal, Y., Ahmed, S., Aziz, M.H., Alam, M., Asif, M., Huang, Q., 2024. Greener approach for the synthesis of Ag decorated ZnO–CeO_2 nanostructure using Moringa oleifera LE and its investigation as photocatalyst for degradation of ciprofloxacin and methylene orange. *Materials Chemistry and Physics*, **318**, 129299. https://doi.org/10.1016/j.matchemphys.2024.129299
26. Tripta, , Rana, P.S., 2023. Structural, optical, electrical, and photocatalytic application of $NiFe_2O_4$@NiO nanocomposites for methylene blue dye. *Ceramics International*, **49**, 13520-13530. https://doi.org/10.1016/j.ceramint.2022.12.227
27. Bopape, D.A., Ntsendwana, B., Mabasa, F.D., 2024. Photocatalysis as a pre-discharge treatment to improve the effect of textile dyes on human health: A critical review. *Heliyon*, **10**, e39316. https://doi.org/10.1016/j.heliyon.2024.e39316
28. Kawsar, M., Sahadat Hossain, M., Tabassum, S., Bahadur, N.M., Ahmed, S., 2024. Synthesis of different types of nano-hydroxyapatites for efficient photocatalytic degradation of textile dye (Congo red): A crystallographic characterization. *RSC Advances*, **14**, 11570-11583. https://doi.org/10.1039/d3ra08527a
29. Nishat, A., Yusuf, M., Qadir, A., Ezaier, Y., Vambol, V., Ijaz Khan, M., Ben Moussa, S., Kamyab, H., Sehgal, S.S., Prakash, C., Yang, H.-H., Ibrahim, H., Eldin, S.M., 2023. Wastewater treatment: A short assessment on available techniques. *Alexandria Engineering Journal*, **76**, 505-516. https://doi.org/10.1016/j.aej.2023.06.054
30. Rashid, R., Shafiq, I., Akhter, P., Iqbal, M.J., Hussain, M., 2021. A state-of-the-art review on wastewater treatment techniques: the effectiveness of adsorption method. *Environmental Science and Pollution Research*, **28**, 9050–9066. https://doi.org/10.1007/s11356-021-12395-x
31. Cestaro, R., Philippe, L., Serrà, A., Gómez, E., Schmutz, P., 2023. Electrodeposited manganese oxides as efficient photocatalyst for the degradation of tetracycline antibiotics pollutant. *Chemical Engineering Journal*, 462, 142202. https://doi.org/10.1016/j.cej.2023.142202
32. Liu, M., Wang, Y., Cheng, Z., Zhang, M., Hu, M., Li, J., 2014. Electrospun Mn_2O_3 nanowrinkles and Mn_3O_4 nanorods: Morphology and catalytic application. *Applied Surface Science*, 313, 360–367. https://doi.org/10.1016/j.apsusc.2014.05.215
33. Ramezanpour, S., Sheikhshoaie, I., Khatamian, M., 2017. Synthesis, characterization and photocatalytic properties of V-doped Mn_3O_4 nanoparticles as a visible light-activated photocatalyst. *Journal of Molecular Liquids*, **231**, 64–71. https://doi.org/10.1016/j.molliq.2017.01.099
34. Zhang, L., Sun, Z., Yao, Z., Yang, L., Yan, N., Lu, X., Xiao, B., Zhu, X., Chen, L., 2020. Excellent catalysis of Mn_3O_4 nanoparticles on the hydrogen storage properties of MgH_2: An experimental and theoretical study. *Nanoscale Advances*, **2**, 1666–1675. https://doi.org/10.1039/D0NA00137F
35. Hu, Z., Zhou, X., Zhang, T., Wu, Z., Li, J., Wang, W., Gao, E., Zhu, J., Yao, S., 2024. Revealing the intrinsic nature of Cu- and Ce-doped Mn_3O_4 catalysts with positive and negative effects on CO oxidation using operando DRIFTS-MS. *Dalton transactions (Cambridge, England : 2003)*, **53**, 16978-16992. https://doi.org/10.1039/d4dt02391a
36. Mandvi; Singh, P.P., Ballal, S., Chahar, M., Bansal, J., Kumar, R., Kumar, S., Kaushal, S., 2024. Construction of a 3D flower-like NiO/Mn_3O_4 heterojunction using Tulsi leaf extract for enhanced photodegradation of thiamethoxam pesticide and organic dyes under direct sunlight. *Materials Advances*, 5, 8097–8110. https://doi.org/10.1039/D4MA00708E
37. Rani, S.J.J., Sinthiya, A.S.I.J., Thangam, G.J.R., Durai, S.C.V., 2024. Synthesis of trimanganese tetraoxide (Mn_3O_4) as a promising electrode and photocatalyst for the degradation of Rhodamine B dye. *Solid State Sciences*, **157**, 107695. https://doi.org/10.1016/j.solidstatesciences.2024.107695
38. Govindana, K., Chandran, H.T., Rajad, M., Maheswari, S.U., Rangarajan, M., 2017. Electron scavenger-assisted photocatalytic degradation of amido black 10B dye with Mn_3O_4 nanotubes: A response surface methodology study with central composite design. *Journal of Photochemistry and Photobiology A: Chemistry*, **341**, 146–156. https://doi.org/10.1016/j.jphotochem.2017.03.025
39. Sheikhshoaie, I., Ramezanpour, S., Khatamian, M., 2017. Synthesis and characterization of thallium doped Mn_3O_4 as superior sunlight photocatalysts. *Journal of Molecular Liquids*, **238**, 248–253. https://doi.org/10.1016/j.molliq.2017.04.088
40. Asif, S.A., Khan, S.B., Asiri, A.M., 2015. Visible light functioning photocatalyst based on Al_2O_3 doped Mn_3O_4 nanomaterial for the degradation of organic toxin. *Nanoscale Research Letters*, **10**, 355. https://doi.org/10.1186/s11671-015-0990-4
41. Srilatha, G., Muralimanohar, P., Sathyamoorthy, K., Vinothkumar, P., Sriram, S., Priya, M., 2020. Investigation on the oxidative capacity of Zn modified Mn_3O_4 nanoparticles by photocatalytic methylene blue dye degradation. *Digest Journal of Nanomaterials and Biostructures*, 15, 895–904. https://doi.org/10.15251/djnb.2020.153.895
42. Uddin, J., Abdur, R., Hossain, M.R., Aziz, S., Jamal, M.S., Shaikh, M.A.A., Hossain, M., 2023. Phase tunable nickel doped Mn_3O_4 nanoparticle synthesis by chemical precipitation: Kinetic study on dye degradation. *Nanoscale Advances*, **6**, 902-909. https://doi.org/10.1039/d3na00754e
43. Prasad, K., Sreekanth, T.V.M., Yoo, K., Kim, J., 2024. Facile synthesis of Mn_3O_4 nanoparticles towards high performance asymmetric supercapacitors. *Vacuum*, **221**, 112930. https://doi.org/10.1016/j.jallcom.2015.02.164
44. Raj, B.G.S., Asiri, A.M., Wu, J.J., Anandan, S., 2015. Synthesis of Mn_3O_4 nanoparticles via chemical precipitation approach for supercapacitor application. *Journal of Alloys and Compounds*, **636**, 234–240. https://doi.org/10.1016/j.jallcom.2015.02.164
45. Arzaee, N.A., Betti, N., Al-Amiery, A., Roslam Wan Isahak, W.N., 2023. The role of tin species in doped iron (III) oxide for photocatalytic degradation of methyl orange dye under UV light. *Heliyon*, **9**, e18076. https://doi.org/10.1016/j.heliyon.2023.e18076
46. Shaik, M.R., Syed, R., Adil, S.F., Kuniyil, M., Khan, M., Alqahtani, M.S., Shaik, J.P., Siddiqui, M.R.H., Al-Warthan, A., Sharaf, M.A.F., Abdelgawad, A., Awwad, E.M., 2021. Mn_3O_4 nanoparticles: Synthesis, characterization and their antimicrobial and anticancer activity against A549 and MCF-7 cell lines. *Saudi journal of biological sciences*, **28**, 1196-1202. https://doi.org/10.1016/j.sjbs.2020.11.087
47. He, Y., Li, J., Tang, J., Cheng, H., Zeng, T., He, Z., Wang, D., Wang, L., Song, S., Ma, J., 2023. Constructed electron-dense Mn sites in nitrogen-doped Mn_3O_4 for efficient catalytic ozonation of pyrazines: Degradation and odor elimination. *Water research*, **247**, 120823. https://doi.org/10.1016/j.watres.2023.120823
48. Zhang, Y., Liang, J., Wu, M., Tang, Q., Xie, Y., Li, Z., Lu, S., Qin, L., Fan, X., 2024. Enhancing aqueous zinc-ion batteries: The role of copper-ion-doped Mn_3O_4 as cathode material. *Materials Today Communications*, **39**, 108942. https://doi.org/10.1016/j.mtcomm.2024.108942
49. Araújo, M.P., Nunes, M., Rocha, I.M., Pereira, M.F.R., Freire, C., 2019. Electrocatalytic activity of new Mn_3O_4@oxidized graphene flakes nanocomposites toward oxygen reduction reaction. *Journal of Materials Science*, **54**, 8919–8940. https://doi.org/10.1007/s10853-019-03508-6
50. Lu, W., Chen, J., Kong, L., Zhu, F., Feng, Z., Zhan, J., 2021. Oxygen vacancies modulation Mn_3O_4 nanozyme with enhanced oxidase-mimicking performance for l-cysteine detection. *Sensors and Actuators B: Chemical*, **333**, 129560. https://doi.org/10.1016/j.snb.2021.129560
51. Cao, L., Du, X., Guo, X., Yuan, Z., 2021. The enhanced electrical transport properties of Fe^{3+} doped Cu_2SnS_3. *Electronic Materials Letters*, **17**, 493–499. https://doi.org/10.1007/s13391-021-00309-5
52. Tang, R., Jiang, C., Qian, W., Jian, J., Zhang, X., Wang, H., Yang, H., 2015. Dielectric relaxation, resonance and scaling behaviors in $Sr_3Co_2Fe_{24}O_{41}$ hexaferrite. *Scientific reports*, **5**, 13645. https://doi.org/10.1038/srep13645
53. Wang, S., Wei, W., Huang, T., Yuan, M., Yang, Y., Yang, W., Zhang, R., Zhang, T., Chen, Z., Chen, X., Shen, G., Dai, N., 2019. Al-doping-induced VO_2 (B) phase in VO_2 (M) toward smart optical thin films with modulated ΔTvis and ΔTc. *Advanced Engineering Materials*, **21**, 1900947. https://doi.org/10.1002/adem.201900947
54. Raji, R., Jyothi, G., Sasidharan, S., Gopchandran, K.G., 2024. White light-emitting ZnO:Dy^{3+} nanophosphors: delving into the spectroscopic parameters via Judd–

Ofelt analysis. *Dalton Transactions*, **53**, 6234–6244. https://doi.org/10.1039/D3DT04070D

55. Patra, T., Panda, J., Sahoo, T.R., 2021. Synthesis of Mn_3O_4 nanoparticles via microwave combustion route for electrochemical energy storage application. *Materials Today: Proceedings*, **41**, 247-250. https://doi.org/10.1016/j.matpr.2020.08.802
56. Ahmed, K.A.M., Huang, K., 2019. Formation of Mn_3O_4 nanobelts through the solvothermal process and their photocatalytic property. *Arabian Journal of Chemistry*, **12**, 429-439. https://doi.org/10.1016/j.arabjc.2014.08.014
57. Dubal, D.P., Dhawale, D.S., Salunkhe, R.R., Fulari, V.J., Lokhande, C.D., 2010. Chemical synthesis and characterization of Mn_3O_4 thin films for supercapacitor application. *Journal of Alloys and Compounds*, **497**, 166-170. https://doi.org/10.1016/j.jallcom.2010.02.182
58. Giri, A., Goswami, N., Pal, M., Zar Myint, M.T., Al-Harthi, S., Singha, A., Ghosh, B., Dutta, J., Pal, S.K., 2013. Rational surface modification of Mn_3O_4 nanoparticles to induce multiple photoluminescence and room temperature ferromagnetism. *Journal of Materials Chemistry C*, **1**, 1885. https://doi.org/10.1039/c3tc00709j
59. Prasanna, V.L., Harikaran, D., Avisar, D., R, V., 2023. Metal peroxides as potential photocatalysts for environmental remediation. *RSC advances*, **13**, 3416-3424. https://doi.org/10.1039/d2ra05754a
60. Ojo, B.O., Arotiba, O.A., Mabuba, N., 2022. Sonoelectrochemical oxidation of sulfamethoxazole in simulated and actual wastewater on a piezo-polarizable FTO/$BaZr_xTi_{(1-x)}O_3$ electrode: Reaction kinetics, mechanism and reaction pathway studies. *RSC Advances*, **12**, 30892–30905. https://doi.org/10.1039/D2RA04876K
61. Rizal, M.Y., Saleh, R., Taufik, A., 2020. Characterization and photocatalytic activity of Ag/Mn_3O_4/graphene composites under visible light irradiation for organic dyes degradation. *Journal of Environmental Chemical Engineering*, **8**, 103610. https://doi.org/10.1016/j.jece.2019.103610
62. Osgouei, M.S., Kamrani, N., Fazli-Shokouhi, S., Khatamian, M., 2022. Improved performance of Mn_3O_4-based nanocomposites in photocatalytic removal of methylene blue. *Journal of Alloys and Compounds*, **902**, 163729. https://doi.org/10.1016/j.jallcom.2022.163729
63. Amin, M.S., Alshareef, F.M., Alsaggaf, W.T., Zaki, Z.I., 2022. Employing manufactured Mn_3O_4–ZnO nanocomposite for ameliorated photocatalytic performance under visible light. *Optical Materials*, **127**, 112286. https://doi.org/10.1016/j.optmat.2022.112286